

# Fractal analysis of crack initiation in polycrystalline alloys using surface interferometry

DEVESH K. JHA<sup>1</sup>, DHEERAJ S. SINGH<sup>1</sup>, S. GUPTA<sup>2(a)</sup> and A. RAY<sup>1</sup>

<sup>1</sup> *Department of Mechanical Engineering, Pennsylvania State University - University Park, PA 16802, USA*

<sup>2</sup> *Department of Electrical and Computer Engineering, University of Connecticut - Storrs, CT 06269, USA*

received 9 January 2012; accepted in final form 24 April 2012

published online 28 May 2012

PACS 46.50.+a – Fracture mechanics, fatigue and cracks

PACS 05.45.Df – Fractals

PACS 62.20.M- – Structural failure of materials

**Abstract** – Microstructural degradation is a predominant source of damage in polycrystalline alloys that are commonly used in diverse applications. For early diagnosis and prognosis of failures, it is essential to understand the mechanisms of damage growth specifically in the crack initiation phase, which is still an intriguing phenomenon for scientists due to sensing inaccuracies and modeling uncertainties. Measurements of gradually evolving deformations on the material surface during crack initiation provide early warnings of forthcoming widespread damage. In this paper, a surface interferometer is used to generate 3-D surface profiles of polycrystalline alloy specimens under oscillating load. The concepts of fractal geometry are used to quantify the changes in the 3-D surface profiles as early indicators of damage evolution in the crack initiation phase.

Copyright © EPLA, 2012

**Introduction.** – Microstructural degradation is a predominant source of damage in polycrystalline alloy structures that are used in diverse applications [1]. The life of these structures subjected to oscillating load patterns is broadly classified into two phases: i) *the crack initiation* and ii) *the crack propagation*. This classification implies that there is a phase transition when microstructural damage in the form of surface and subsurface deformities (*e.g.*, voids, slip bands, inclusions, casting defects, machining marks, and dislocations) develop into multiple micro-cracks, that in turn coalesce together to develop into a single large crack that propagates under oscillating load [1]. Therefore, for early diagnosis and prognosis of failures, it is essential to understand the mechanisms of damage growth specifically in the *crack initiation phase*, which is still an intriguing phenomenon for scientists due to sensing inaccuracies and modeling uncertainties. In the current state-of-the-art, early diagnosis in the crack initiation phase is a critical challenge. Furthermore, fatigue damage evolution is critically dependent on the initial defects present in the materials, which may form random crack nucleation sites [2]. This random distribution of microstructural flaws may produce a wide uncertainty in the crack initiation phase under similar loading conditions [3], thereby making damage evolution a stochastic

phenomenon. Since accurate identification of exact initial conditions is infeasible, sole reliance on model-based analysis in the crack initiation phase is inadequate due to lack of requisite modeling accuracy [4,5].

Many model-based techniques have been reported in the literature. Qian *et al.* [6] did a X-ray computed microtomography study of the ductile fracture process of an aluminum alloy. Stochastic approaches have been developed for modeling 2D crack propagation in heterogeneous materials [7] and characterization of surface profiles [8]. Some studies attempted to model short cracks [9] while others correlated the mechanical properties of materials with the fractured surfaces [10,11]. Apparently, no existing model, solely based on the fundamental principles of physics, can adequately capture the dynamical behavior of damage evolution in the crack initiation phase.

Alternatively, data-driven techniques have been proposed based on different sensing devices (*e.g.*, acoustic emission [12], eddy currents [13] and ultrasonics [14,15]). While each of these methods has its own limitations, ultrasonic sensing has been proven to be one of the most successful methods for early detection of subsurface damage during crack initiation, when no surface damage is visible on a typical (100×) optical microscope. This paper complements the prior work on ultrasonic sensing [3,15] by studying the surface phenomenon that occurs during crack initiation using the surface interferometry.

<sup>(a)</sup>E-mail: shalabh.gupta@engr.uconn.edu

Technical literature abounds with studies where the concepts of fractal geometry [16] have been used to investigate the fundamental properties of complex systems in a diverse range of scientific disciplines. For example, time series analysis [17,18], fracture mechanics [19–21], earthquake modeling [22], material surfaces [23–25], medical imaging [26], financial markets [27], and percolation in porous media [28]. Mandelbrot *et al.* showed that fractured surfaces are fractals in nature whose fractal dimension correlates with the toughness of the material [29]. Lung *et al.* [30] studied the relationship between the fractal dimension and the roughness of surfaces. Bouchaud *et al.* [31] developed models of small fractal-type cracks. Canessa and Tanatar [32] developed a model of multi-branched crack growth using fractal geometry.

The above attempts have been made to study the fractal surfaces when short to large range cracks have already appeared on the surface. In particular, the existing literature has mainly focused on the fractal-based modeling of short cracks [33] and fractured surfaces of brittle materials [34]. However, the study of gradual evolution of surface deformations in the crack initiation phase in ductile materials, which ultimately leads to fully developed rapidly propagating cracks, has not been reported. In this regard, the contributions of this paper are as follows:

- Experimentation and measurement of surface deformations during crack initiation using a surface interferometer and generation of 3-D surface profiles data.
- Analysis of surface data using methods of fractal geometry for damage characterization and to generate early warnings of forthcoming widespread damage.

**Experimental description.** – A NewView 5000 surface interferometer, as shown in fig. 1, has been used to generate the 3-D surface profiles of specimens subjected to cyclic loading patterns. The interferometer measures the surface heights ranging from 1 nm to 5000  $\mu\text{m}$  with a resolution of 0.1 nm at the vertical scan speeds of up to 10  $\mu\text{m}/\text{s}$ . It uses a closed-loop piezoelectric scanner employing low-noise capacitive sensors to ensure accurate and repeatable linear motion over the full range of scanned area. The interferometer can scan areas up to 50 mm  $\times$  50 mm using its unique stitching capabilities and generates ultrahigh resolution surface profiles using a non-contact scanning method based on white light interferometry principle. Light from the microscope is divided within the interferometric objective, where one portion reflects from the test surface and the other portion reflects from an internal high quality reference surface in the objective. Both light wavefronts are directed onto a solid state camera leading to interference that generates fringes, which indicate the characteristics of the surface being tested. Finally, the surface profiles are generated as 3-D profiles, where two of these dimensions represent the scanned area and the third dimension represents the

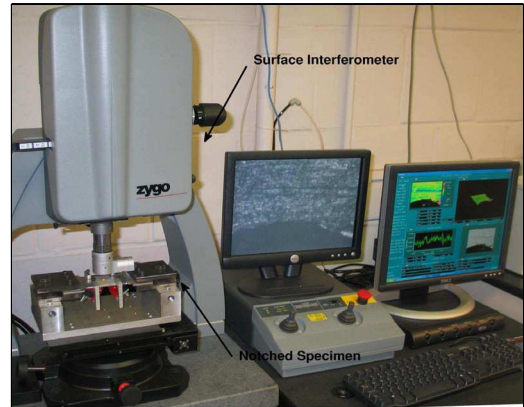


Fig. 1: (Colour on-line) The surface interferometer.

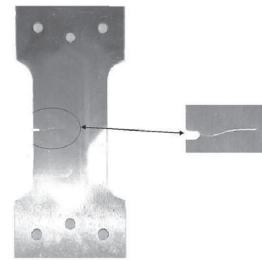


Fig. 2: A typical (cracked) side-notched test specimen.

pixel values that are isomorphic to the height of the local region.

The test specimens, made of 2024-T6 aluminum (a typical polycrystalline alloy), are 3 mm thick, 50 mm wide and have a side notch of 1.58 mm  $\times$  4.57 mm as seen in fig. 2. The notch is made to increase the stress concentration to ensure crack initiation and propagation around the notch. The specimens have been subjected to tensile-tensile cyclic loading on an MTS 831.10 Elastomer system at a frequency of 100 Hz such that the far-field stress oscillates between 86.67 MPa and 3.33 MPa (*i.e.*, with a peak to valley ratio of 26). The ratio of the peak stress to the ultimate tensile strength (476 MPa) is  $\sim 0.18$ . The specimen surfaces have been observed under the interferometer after every 7.5 kilocycles of the oscillating load.

The physical phenomena of surface deformation are, in general, qualitatively similar in different polycrystalline alloys due to fatigue damage under cyclic (tensile) stresses, provided that the environmental temperature is well below approximately one third of the melting point of the material [1]. The results of experimentation, reported in this paper, are expected to be qualitatively similar to the fatigue damage behaviors of other polycrystalline alloys. The specimen surface is subjected to monotonically increasing deformation due to grain dislocations within the specimen. As precursors to the appearance of a crack on the surface, these phenomena culminate as waviness on the surface that is captured by interferometry.

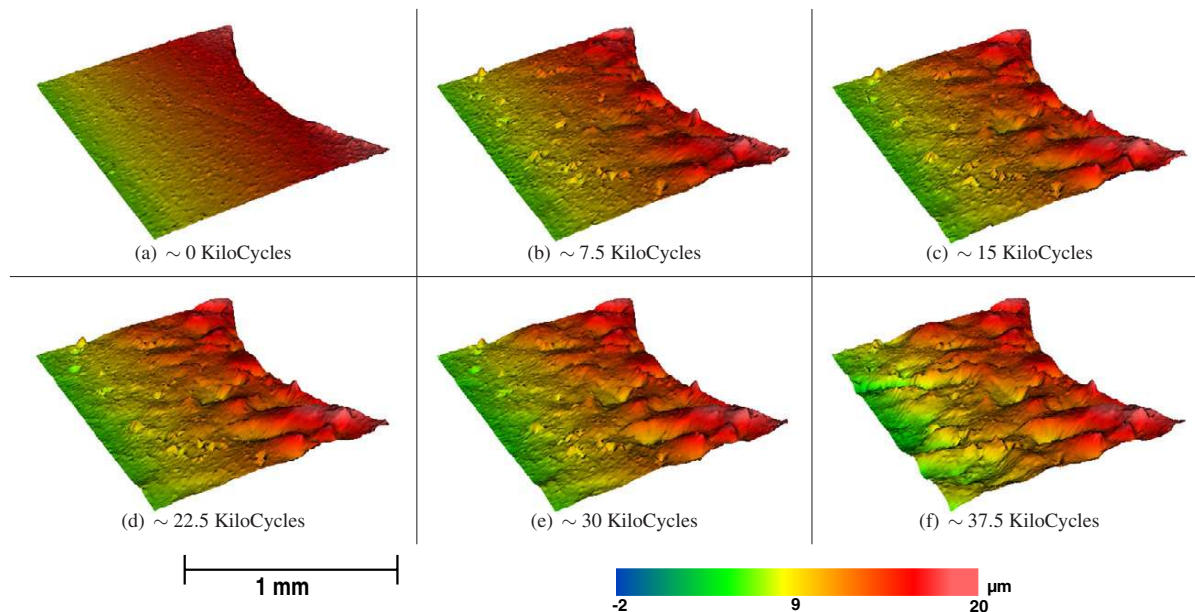


Fig. 3: (Colour on-line) Evolution of the surface deformation with microstructural damage.

Figure 3 shows the 3-D profiles of the specimen surface near the notch for six different time epochs, each separated by 7.5 kilocycles. As seen in fig. 3, surface deformation is more prominent around the notch due to high stress concentration. The six plots in fig. 3 show the gradual spatio-temporal evolution of the surface deformations in the crack initiation phase. While the plot in fig. 3(a) shows a healthy (polished) specimen surface, the plot in fig. 3(f) shows widespread surface damage that eventually developed into a rapidly propagating crack. Transitions from the crack initiation phase to the crack propagation phase occurred in the vicinity of 37.5 kilocycles in all specimens under this cyclic loading. Since the fatigue life in the crack propagation phase is governed by significantly different physical phenomena, this issue is not addressed in this paper; results of fatigue life prediction in the crack propagation phase are reported elsewhere [3,35].

**Fractal analysis.** – Mandelbrot illustrated that roughness cannot be studied using general topological notions and demands an altogether different toolbox, called *fractal geometry* [16]. The basic principle to estimate fractal dimension is based on the concept of self-similarity. Consider a non-empty bounded subset  $F$  in the Euclidean space  $\mathbb{R}^n$ , where  $n \in \mathbb{N}$ . The set  $F$  is said to be self-similar when  $F$  is the union of  $N(r)$  distinct (non-overlapping) copies of itself each of which is similar to  $F$  scaled down by a ratio  $r$ . The most popular way to calculate the fractal dimension is by box-counting [36]. Let  $N(r)$  be the smallest number of sets of diameter  $r$ , with  $0 < r \ll 1$ , which covers  $F$ . Then, the lower and upper box dimensions of  $F$  are, respectively, defined [37] as follows:

$$\underline{D}_F \triangleq \liminf_{r \rightarrow 0^+} \frac{\log_2 N(r)}{-\log_2 r} \quad \text{and}$$

$$\overline{D}_F \triangleq \limsup_{r \rightarrow 0^+} \frac{\log_2 N(r)}{-\log_2 r}.$$

If the above two limits are equal, then the box dimension  $D_F$  of  $F$  is defined as

$$D_F \triangleq \lim_{r \rightarrow 0^+} \frac{\log_2 N(r)}{-\log_2 r}. \quad (1)$$

The box-counting approach to compute the fractal dimension yields a systematic procedure that applies to any structure in a texture plane and can be adapted for structures in multi-dimensional spaces. For 3-D surface profiles, the idea of this approach is to partition the (3-D) data with regular cubic boxes with each side of size  $r$ . The grid is progressively made finer by reducing  $r$  and thus the number  $N(r)$  increases. The fractal dimension is obtained as the slope of the straight line, as shown in fig. 4(a). One advantage of the fractal analysis method is that it provides a measure of absolute damage as compared to some other methods that provide a relative measure by comparison of the current observed pattern with the nominal pattern [3].

The surface profiles obtained from the interferometer are preprocessed before using the box-counting algorithm. The pre-processing is done for: i) filtering noisy data, ii) filling the vacant (*i.e.*, unmeasured) points, and iii) mitigating the effects of orientation of the specimen. The details of these methods are omitted for brevity. Image registration is done to make sure that data from the same region on the specimen surface is analyzed, by fitting the notch edge with a circular arc and finding the coordinates of the center. The center and the notch of each image are matched by translation and rotation. Finally, a rectangular region of  $1024 \times 1024$  pixels ( $\sim 0.64 \text{ mm} \times 0.64 \text{ mm}$ ) is clipped from each image for further analysis.

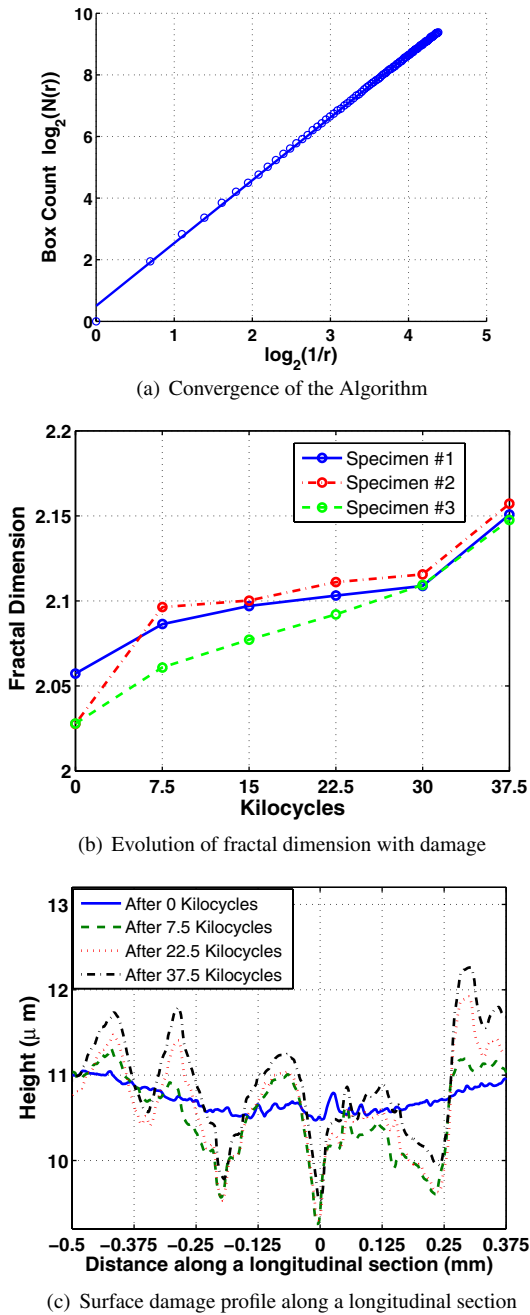


Fig. 4: (Colour on-line) Fractal analysis of the surface deformation profiles.

Figure 4(b) shows the evolution of fractal dimension at different time epochs for three different specimens. The fractal dimension increases with the surface damage, which is consistent with the damage evolution observed in fig. 3. The curves in fig. 4(b) can be broadly classified into three distinct regions: i) the initial region of sharp increase in the fractal dimension, ii) the middle region that forms a plateau of slowly evolving changes, and iii) the final region that shows a sharp increase in the fractal dimension. These observations are explained as follows. Initially, when

the specimen is loaded for the first time, there is an appreciable change in the surface profile. After that there is a phase of dormancy, when not much change is observed in the surface profile. This is followed by widespread surface damage that leads to a phase transition to the crack propagation phase. During the initial loading cycles, the atomic structure of the specimen is well-organized and the surface is polished. Thus, rapid deformations occur during the initial few cycles. Subsequently, with the formations of multiple slip bands and dislocations, the surface becomes hard and further damage growth is slowed down. Finally, after a sufficient number of cycles, when the effects of hardening are overcome, the surface deformations begin to grow at a rapid pace and lead to a phase transition when multiple micro-cracks form that in turn coalesce to form a single macro-crack that is visible on a standard optical microscope.

A higher fractal dimension for a surface means greater amount of space it occupies in a compact 3-D space. A surface X is rougher than a surface Y if X has more singular (*i.e.*, non-differentiable) points than Y, in other words, X has a higher fractal dimension than Y [16]. Figure 4(c) shows the surface profiles at a particular longitudinal section close to the notch, at four different time epochs: i) a fresh specimen, ii) 7.5 kilocycles, iii) 22.5 kilocycles, and iv) 37.5 kilocycles. The surface profile of the fresh specimen is smooth with small kinks due to polishing imperfections. The evolution of these profiles show how the roughness increases with damage as time progresses.

**Lacunarity analysis.** – Lacunarity analysis is a multi-scale method of determining spatial dispersion, *i.e.*, the deviation of a geometric object, such as a fractal, from translational invariance [38,39]. Translationally invariant objects, that are homogeneous (*i.e.*, all gaps sizes being the same), have low lacunarity. In contrast, translationally non-invariant objects, that are heterogeneous (*i.e.*, a wide range of gap sizes), have high lacunarity. Note that translational invariance is scale-dependent, *i.e.*, objects that are heterogeneous at small scales may look homogeneous at larger scales and vice versa.

Lacunarity is computed using the gliding box algorithm [40]. Figure 5 shows examples of three  $8 \times 8$  maps with their lacunarity values. Lacunarity is computed by sliding a box of size  $r \times r$  (*e.g.*,  $r = 2$ ) on the map by moving it by one cell at a time. The number of occupied sites (*i.e.*, symbol 1) within the box, called the *box mass*, is counted for each position over all rows and columns to get the frequency of box masses. The number of boxes of size  $r$  with  $k$  occupied sites is denoted by  $n(k, r)$  and the total number of boxes is denoted by  $N(r)$ . For an  $M \times M$  map,  $N(r) = (M - r + 1)^2$ . The probability distribution of the box mass is given as  $P(k, r) = n(k, r)/N(r)$ . The first and the second moments of the probability distribution  $P(k, r)$  are obtained as  $Z_1(r) = \sum_k kP(k, r)$  and  $Z_2(r) = \sum_k k^2P(k, r)$ , respectively. The lacunarity is

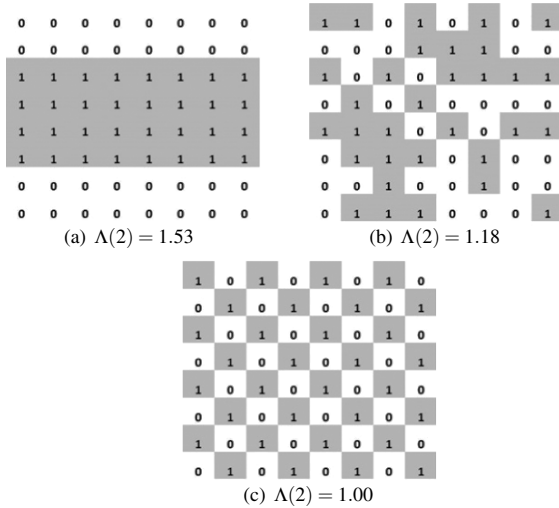


Fig. 5: Examples of lacunarities of three  $8 \times 8$  maps.

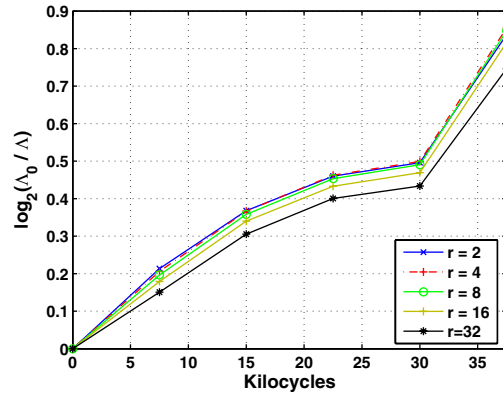
defined as

$$\Lambda(r) = Z_2(r)/Z_1^2(r). \quad (2)$$

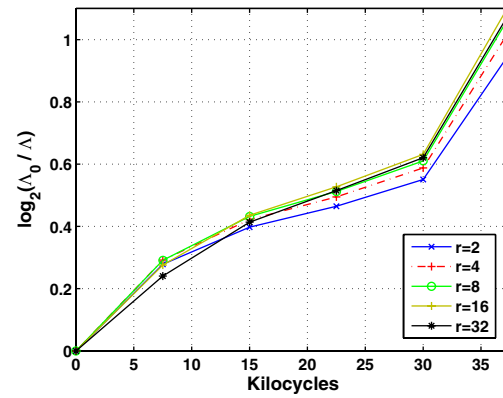
In general, sparse maps have higher lacunarities than dense maps, for the same gliding box. Also higher lacunarity indicates greater clumping. Figure 5(a) shows a map with a large patch of occupied cells, with  $\Lambda(2) = 1.53$ . Figure 5(b) shows a random map with  $\Lambda(2) = 1.18$ , where the probability of occupancy of a cell is  $p = 0.5$ . Figure 5(c) shows a perfectly regular map with  $\Lambda(2) = 1.00$ . The algorithm can be easily extended to multi-dimensional data.

For lacunarity analysis, the surface profiles (see fig. 3) are converted into 3-D binary data sets by partitioning. A window of size  $1024 \times 1024$  pixels ( $\sim 0.64 \text{ mm} \times 0.64 \text{ mm}$ ) is selected near the notch. The range of the surface height at each pixel is divided into 512 segments, which yields a 3-D cellular structure of size  $1024 \times 1024 \times 512$ . A cell is labeled with a 1 if a data point falls in any of the cells directly above it; otherwise, it is labeled with a 0. Lacunarity of these data sets are calculated for different box sizes ( $r$ ).

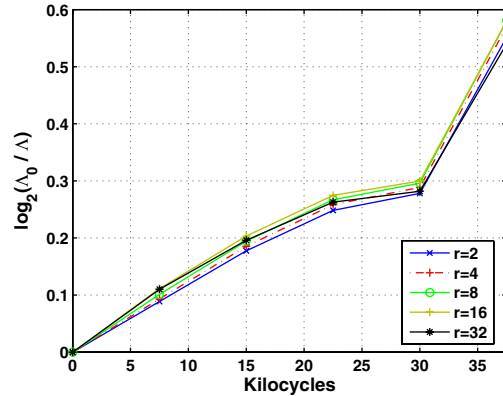
The three plots in fig. 6 show the evolution of lacunarity at different time epochs for three different specimens, respectively. Lacunarity of the surface profile of a damaged specimen is normalized relative to the initial value of lacunarity ( $\Lambda_0$ ), *i.e.*, lacunarity of the surface with no damage. Each plot in fig. 6 shows the curves of  $\log_2(\Lambda_0/\Lambda)$  vs. the load cycles for different box sizes  $r = 2, 4, 8, 16$  and 32. All these curves show similar trend of decreasing lacunarity (*i.e.*, increasing  $\log_2(\Lambda_0/\Lambda)$ ) with increasing load cycles. A smoother surface has a higher lacunarity because the material is concentrated in the lowest segments of the partition. In contrast, a rougher surface is distributed in the entire range of the surface height and results in lower lacunarity. Furthermore, it is observed that the lacunarity of a surface profile is invariant with respect to the scale size, which confirms its fractal nature [38].



(a) Evolution of lacunarity for Specimen#1



(b) Evolution of lacunarity for Specimen#2



(c) Evolution of lacunarity for Specimen#3

Fig. 6: (Colour on-line) Lacunarity analysis of the surface profiles at different scales.

The lacunarity plots suggest that the surface deformation rate is maximum at the beginning of the damage process and as damage increases, the rate of change in surface deformation decreases. This phenomenon is explained in terms of strain hardening in low-cycle fatigue. As loading starts, the material near the notch undergoes plastic deformation due to a high stress-concentration factor causing strain hardening [1], that in turn reduces the damage rate. The sudden change in the slope of lacunarity in all three specimens, as seen in the three plots

of fig. 6, at 30 kilocycles indicates the onset of a phase transition from crack initiation to crack propagation; this observation is in agreement with the evolution of fractal dimension in fig. 4(b). At this point the material becomes abruptly weaker. It is to be noted that, during the middle phase of crack initiation, the fractal dimension does not change significantly; however, the upward slope of lacunarity in this region suggests that the surface texture (*i.e.*, the distribution of peaks and valleys) changes even when a dormant phase is seen in terms of fractal dimension.

**Conclusions and future work.** – This paper presents an analysis of the evolution of surface deformations in polycrystalline alloys during crack initiation using the methods of fractal geometry. White light interferometry has been used to measure the 3-D surface topologies of aluminium specimens. It has been found that as the surface deforms, its fractal dimension increases and the lacunarity decreases. The nature of the fractal dimension and lacunarity curves provides insights into surface roughening behavior during crack initiation. The following topics are recommended for future research: i) multifractal analysis of the surface during crack initiation and ii) Calibration of the results of fractal analysis with ultrasonic sensors for online recursive estimation of remaining life.

\*\*\*

This work has been supported in part by the U.S. Army Research Laboratory and the U.S. Army Research Office under grant No. W911NF-07-1-0376. Any findings and opinions of this paper are those of the authors and do not necessarily reflect the views of the sponsoring agencies. The first two authors have equal contributions.

## REFERENCES

- [1] SURESH S., *Fatigue of Materials* (Cambridge University Press) 1998.
- [2] SOBCZYK K. and SPENCER B. F., *Random Fatigue: Data to Theory* (Academic Press, Boston, Mass.) 1992.
- [3] GUPTA S. and RAY A., *Meas. Sci. Technol.*, **18** (2007) 1947.
- [4] GUPTA S. and RAY A., *J. Stat. Phys.*, **134** (2009) 337.
- [5] RAY A., *Signal Process.*, **84** (2004) 1115.
- [6] QIAN L. and TODA H., *Appl. Phys. Lett.*, **87** (2005) 241907.
- [7] KATZAV E., ADDA-BEDIA M. and DERRIDA B., *EPL*, **78** (2007) 46006.
- [8] WAECHTER M., RIESS F., KANTZ H. and PIENKE J., *EPL*, **64** (2003) 579.
- [9] ISHIHARA S. and MCEVILY A. J., *Inter. J. Fatigue*, **24** (2002) 1169.
- [10] GABRIELLI A., CAFEIRO R. and CALDARELLI G., *Europhys. Lett.*, **45** (1999) 13.
- [11] HERRMANN H. J., KERTSÉSZ J. and ARCANGELIS L., *Europhys. Lett.*, **10** (1989) 147.
- [12] LYSAK M. V., *Eng. Frac. Mech.*, **55** (1996) 443.
- [13] ZILBERSTEIN V., WALRATH K., GRUNDY D., SCHLICHER D., GOLDFINE N., ABRAMOVICI E. and YENTZER T., *Int. J. Fatigue*, **25** (2003) 1147.
- [14] ROKHLIN S. I. and KIM J.-Y., *Int. J. Fatigue*, **25** (2003) 41.
- [15] GUPTA S., RAY A. and KELLER E., *Mech. Syst. Signal Process.*, **21** (2007) 866.
- [16] MANDELBROT B. B., *The Fractal Geometry of Nature* (W. H. Freeman and Company, New York) 1983.
- [17] GOLESTANI A., JAHED MOTLAGH M. R., AHMADIAN K., OMIDVARNIA A. H. and MOZAYANI N., *Chaos*, **19** (2009) 013137.
- [18] BILLAT V. L., MILLE-HAMARD L., MEYER Y. and WESFREID E., *Physica A*, **388** (2009) 3798.
- [19] CHARKALUK E., BIGERELLE M. and IOST A., *Eng. Fract. Mech.*, **61** (1998) 119.
- [20] AUSLOOS M. and KOWALSKI J. M., *Phys. Rev. B*, **45** (1992) 12830.
- [21] CARPINTERI A. and SPAGNOLI A., *Int. J. Fatigue*, **26** (2004) 125.
- [22] CHAKRABARTI B. K. and STINCHCOMBE R. B., *Physica A*, **270** (1999) 27.
- [23] CHOU C. C. and LIN H. H., *J. Appl. Phys.*, **107** (2010) 073510.
- [24] QUARTARONE E., MUSTARELLI P., POGGIO C. and LOMBARDINI M., *J. Appl. Phys.*, **103** (2008) 104702.
- [25] MARX D. T., KHOR E. and POLICANDRIOTES T., *J. Appl. Phys.*, **100** (2006) 124913.
- [26] MANSURYA Y. and DEISBOECKA T. S., *Physica A*, **331** (2004) 219.
- [27] MOYANO L. G., DE SOUZA J. and QUEIROS S. M. D., *Physica A*, **371** (2006) 118.
- [28] XU Y. F. and SUN D. A., *Physica A*, **316** (2002) 56.
- [29] MANDELBROT B. B., PASSOJA D. E. and PAULLAY A. J., *Nature*, **308** (1984) 721.
- [30] LUNG C. W., JIANG J., TIAN E. K. and ZHANG C. H., *Phys. Rev. E*, **60** (1999) 5121.
- [31] BOUCHAUD J. P., BOUCHAUD E., LAPASSET G. and PLANES J., *Phys. Rev. Lett.*, **71** (1993) 2240.
- [32] CANESSA E. and TANATAR B., *Phys. Rev. A*, **44** (1991) 3471.
- [33] SPAGNOLI A., *Mech. Mater.*, **37** (2005) 519.
- [34] ZHU M., LI W., FANG Y., ZHANG W., ZHAO R., WANG J., LI A., FENG H., GUO Z., ZHOU M. and LI Y., *J. Appl. Phys.*, **109** (2011) 07A706.
- [35] SINGH D. S., GUPTA S. and RAY A., to be published in *Struct. Health Monit.* (2012) doi: 10.1177/1475921711432003.
- [36] SARKAR N. and CHAUDHURI B. B., *IEEE Trans. Syst. Man Cybern.*, **24** (1994) 115.
- [37] FALCONER K., *Fractal Geometry, Mathematical Foundations and Applications*, second edition (John Wiley and Sons Ltd., West Sussex, England) 2003.
- [38] ALLAIN C. and CLOITRE M., *Phys. Rev. A*, **44** (1991) 3552.
- [39] GEFEN Y., MEIR Y., MANDELBROT B. B. and AHARONY A., *Phys. Rev. Lett.*, **50** (1983) 145.
- [40] PLOTNICK R. E., GARDNER R. H. and O'NEILL R. V., *Landsc. Ecol.*, **8** (1993) 201.